Solubility of monoclinic and yttrium stabilized cubic ZrO_2: Solution and surface thermodynamics guiding ultra-trace analytics in aqueous phase

W. Zouari, Tomo Suzuki-Muresan, T. Kobayashi, S. Utsunomiya, A. Abdelouas, Bernd Grambow

Solubility of monoclinic and yttrium stabilized cubic ZrO_2: solution and surface thermodynamics guiding ultra-trace analytics in aqueous phase

W. ZOUARI [1], T. SUZUKI-MURESAN [1,], T. KOBAYASHI [2], S. UTSUNOMIYA[3], A. ABDELOUAS [1] and B. GRAMBOW [1]*

[1] SUBATECH, Unité Mixte de Recherche 6457, IMT Atlantique, CNRS/IN2P3, Université de Nantes, 4 rue Alfred Kastler, BP 20722, 44307 Nantes cedex 03, France

[2] Department of Nuclear Engineering, Kyoto University, Kyotodaigaku-katsura, Nishikyo-ku, Kyoto 615-8540, Japan

[3] Department of Chemistry, Kyushu University, 744 Motooka, Nishi-ku, Fukuoka, 819-0395, Japan

ABSTRACT. The high stability of zirconium dioxide in aqueous environments is known and demonstrated, and this property is strongly used in nuclear industry to ensure the long term storage of wastes. However, only upper limits of its aqueous solubility are known reliably and lower limits linked to very well crystallized ZrO_2 are much less assessed. Indeed, the low dissolution rate of zirconia makes the solubility measurements a challenging task. To overcome, high S/V ratios of nanoparticles zirconia were used. This work also improved the sensitivity of analytical techniques (HR ICP-MS) and methodologies, and a reliable experimental procedure was developed to measure zirconium (quantification limit $\approx 10^{-11}$ mol·L^{-1}). New Zr(IV) dioxide solubility data at pH between 0 and 2 were obtained approaching solubility from under-saturated conditions in (Na,H)Cl and (Na,H)ClO_4 medium. Two crystalline nanoparticle structures were compared: monoclinic and yttrium stabilized cubic zirconia. Very low solubility was measured for monoclinic phase between pH 1.5 and 2: between (1.8±1.2)×10^{-10} mol·L^{-1} at pH 2 and (2.3±1.0)×10^{-10} mol·L^{-1} at pH 1.5. The cubic zirconia showed higher solubility. Integrating the effect of ionic strength, particle size and aqueous speciation, solubility constants of log K_s^0 = (-8.43±0.69) for the monoclinic nanoparticles and log K_s^0 = (-7.12±0.35) for the yttrium stabilized cubic nanoparticles were obtained. High-resolution techniques (HR-TEM, SAXS and STEM-HAADF) were also used to assess the evolution of morphology and surface before, during and at equilibrium. Analysis of these results shows that the morphology and surface of nanoparticles in the raw state and after reaching equilibrium in (Na,H)Cl and (Na,H)ClO_4 medium are similar.

KEYWORDS: zirconia, solubility, thermodynamic, ultra-trace analyses, nanoparticles

Corresponding author: suzuki@subatech.in2p3.fr

1 Introduction

ZrO_2 zirconia is a natural mineral named Baddeleyite used in various domains for its excellent physical, chemical, and thermal properties [1–3]. Zirconia is also the corrosion product by oxidation of Zr-based materials, and in nuclear fields, it is omnipresent as a tight oxidation film at surfaces of nuclear fuel claddings. This oxide layer is considered as a protective layer in zirconium alloys, enhancing the corrosion resistance of the claddings in the reactor vessel as well as in the wet pool of deactivation. It is noteworthy that this layer is exposed to several combined constraints under extreme conditions such as high gradient of temperature, high pressure, mechanical stress and radiolysis. The characterization of this layer show a very good stability and corrosion resistance in water for temperatures as high as 400°C for many years and for high burnup [4]. The microstructure of the oxide layer reveals an arrangement of small oxide grains of about 30nm, which elongate to form columns of about 200nm [4]. The stability of this oxide layer is thus ensured by a dense growth of nanometric size zirconia grains. However, the stability of nanoparticles strongly depends on the surface energy and solubility which increases when particle size decreases [5,6]. Therefore, an appropriate knowledge of the solubility of waste form constituents is required for the safety of disposal of nuclear waste in geological repository systems.

The solubility of actinide and metallic oxides confining radioactive waste has been studied in these last decades using several analytical methods [7]. However, the reported solubility values are contradictory with large uncertainties mostly due to changes in the characteristics of the solid phases: crystallinity, composition and particle size, chemical reactions occurring on solid phases during the experiment and the presence of colloids in solution. Of the tetravalent oxides, crystalline zirconium dioxide is a strong refractory material leading to high corrosion resistance in acidic, neutral and alkaline media. Therefore its solubility is very low ($<10^{-8}$ mol·L^{-1}) between pH 3 and 12, increasing at more acidic and alkaline pH (Figure 1). Solubility values are reported to differ by more than 6 orders of magnitude comparing results from over- and under-saturated conditions. Furthermore, solubility data are influenced by the formation of polynuclear species in solution and by the precipitation reaction occurring even at low pH [8]. Up to date, a wide number of zirconium dioxide solubility studies have been reported in literature as function of pH [8–19], media [8,9,11,13,14,17,19], and crystallographic structure [11,14]. It appears that crystalline zirconium dioxide is the solubility controlling phase in natural water at low temperature (T < 1420K) [20]. Solubility values are generally measured by ICP–MS [8,11,12,15,21] and by potentiometric titration [8], but only few characterizations by X-ray diffraction (XRD) and Laser Induced Breakdown Detection (LIBD) are available for the studied solids [8,10,12]. Reversibility of supposed solubility equilibrium values are hardly ever tested. Difficulties in measuring reversibility are because precipitated phases

might be amorphous while the dissolved one is crystalline. A solubility constant of (log K_s^0 (monoclinic ZrO_2, 298.15K) = –(7.0±1.6) (eq. (1)) was selected by Brown et al. [20] in their review focusing on the low-temperature thermodynamics of zirconium and its compounds in aqueous solution. This constant is obtained from an overall fit of hydrolysis data with a detailed review of hydrolysis of zirconium in the aqueous phase and its ionic strength dependency. The selected solubility constant of the freshly precipitated amorphous hydroxides is log K_s^0 (amorphous $Zr(OH)_4$, 298.15K) = –(3.24±0.10). The lack of detailed characterization of the studied zirconium dioxide materials may impact on the accuracy of the free energy of formation ($\Delta_f G°$) of the aquo–ion Zr^{4+} derived by Brown et al. from the equilibrium (1):

ZrO_2 (monoclinic) + $4H^+ = Zr^{4+} + 2\ H_2O$ (eq.1)

The thermodynamic properties calculated by Brown et al. [20] vary with the degree of crystallinity of the zirconium oxide in equilibrium with dissolved Zr^{4+}.

The aim of the present paper is to assess zirconia solubility of two crystalline polymorphs varieties, the monoclinic and the yttrium stabilized cubic zirconia phases. The purpose is also to assess the surface reactivity of the solid since the reversibility cannot be studied by comparing results of approaching solubility from under and over-saturation due to the different phases. Finally, the solubility constant (log K_s^0(298 K)) obtained at solubility equilibrium on crystalline zirconium oxide will be discussed and compared with solubility constant values of amorphous hydrous oxide of zirconium.

2 Experimental

2.1 Solubility experiment.

Solubility experiments of monoclinic zirconium (IV) oxide (MZ) and cubic zirconium (IV) oxide (YSZ, yttrium-stabilized zirconia up to 8 mol%) nanoparticles (Sigma-Aldrich) were performed in Teflon reactor vessels with 120 mL of 10^{-2} mol·L^{-1} NaCl or $NaClO_4$ solutions. The ratio surface area of solid over volume of solution (S/V) varied between 10^4 and 2×10^6 m^{-1}. Table 1 summarizes in detail the experimental conditions. To minimize any contamination source of zirconium, sodium perchlorate, sodium chloride, hydrochloric acid, perchloric acid are ultra-pure chemical solutions and prepared with ultrapure water from a water purification apparatus (Milli-Q-academic, Millipore). The reactors were cleaned by several washings with HNO_3, HCl and Milli-Q water at 100 °C to avoid the release of Zr traces from material prior to use. Nitric acid is ultra-pure chemical and is distilled in laboratory to reduce traces of zirconium. An orbital stirrer at room temperature and under atmospheric conditions continuously shook the reactors.

As the dissolution rate of ZrO_2 is very slow, it may take a long time until solubility equilibrium is reached. The use of nanoparticles of high specific surface area decreases the time until equilibrium is achieved. Therefore, the S/V ratio was varied to follow the approach to equilibrium and to ensure that solid/liquid equilibrium has been reached. The determination of surface area is described in solid characterization section. Two approaches were used:

- Approach of equilibrium from undersaturation: the solids dissolve slowly and it takes long time to reach constant solution concentrations. The use of a high S/V speeds up the approach of equilibrium from undersaturated conditions since at concentrations much lower than concentrations at saturation (or at solubility equilibrium), the accumulation rate of dissolved Zr in solution is proportional to the area of the dissolving surface for a given solution volume.
- Approach of equilibrium from oversaturation: in particular in strongly acidic conditions, the dissolution rate may be fast and precipitation or growth rates slow and instead of establishing equilibrium, solution concentrations increase beyond the equilibrium state. With longer dissolution times, solution concentrations decrease again and the intervening precipitation or particle growth reaction approaches equilibrium from oversaturation. The use of high surface area to volume ratio allows in this case a rapid approach of equilibrium since a larger surface is available to adsorb the excessively dissolved Zr providing that no new particles are formed.

For the determination of solubility values, Zr concentration ($[Zr]_{tot}$) data are plotted as function of the product "S/V ratio" and "time", i.e. (S/V)×t. This representation allows determining zirconium solubility data for a given phase under the same pH and media conditions. For a sufficiently long experiment duration and for high S/V ratios, it becomes possible to determine a mean solubility value. The uncertainty associated corresponds to the standard deviation of the values chosen to calculate the mean solubility value.

According to the hydrolysis model, zirconium solubility can be described as the contribution of zirconium species in solution at pH [0-2] and as the function of hydrolysis constants:

$$[\mathrm{Zr}]_{\mathrm{tot}} = [\mathrm{Zr}^{4+}] + [\mathrm{ZrOH}^{3+}] + [\mathrm{Zr(OH)}_2^{2+}] + [\mathrm{Zr(OH)}_4^0(\mathrm{aq})] + [\mathrm{Zr}_3(\mathrm{OH})_9^{3+}] + [\mathrm{Zr}_4(\mathrm{OH})_8^{8+}]$$

$$= K_s[\mathrm{H}^+]^4 \left(1 + \frac{{}^*\beta_{1,1}}{[H^+]} + \frac{{}^*\beta_{2,1}}{[H^+]^2} + \frac{{}^*\beta_{4,1}}{[H^+]^4}\right) + K_S^3[H^+]^3\ {}^*\beta_{9,3} + K_S^4[H^+]^8\ {}^*\beta_{8,4}$$

where Ks represents the solubility constant and ${}^*\beta_{q,\mathrm{m}}$ the hydrolysis constant with (q,m) referring to the general hydroxyl specie $\mathrm{Zr_m(OH)_q^{4m-q}}$ from to the zirconium hydrolysis model. The hydrolysis constants are determined according to the specific ion interaction theory SIT. The values selected

from [20] are: (i) for hydrolysis constants log ${}^{*}\beta^{\circ}_{1,1}$= (0.32±0.22), log ${}^{*}\beta^{\circ}_{2,1}$= (0.98±1.06), log ${}^{*}\beta^{\circ}_{4,1}$= -(2.19±1.70), log ${}^{*}\beta^{\circ}_{9,3}$= (12.19±0.08), and log ${}^{*}\beta^{\circ}_{8,4}$= (6.52±0.65); (ii) for ion interaction coefficients $\varepsilon(Zr^{4+}, ClO_4^-)$ = 0.89 kg·mol^{-1}, $\varepsilon(ZrOH^{3+}, ClO_4^-)$ = 0.57 kg·mol^{-1}, $\varepsilon(Zr(OH)_2^{2+}, ClO_4^-)$ = 0.62 kg·mol^{-1}, $\varepsilon(Zr_3(OH)_9^{3+}, ClO_4^-)$ = 0.93 kg·mol^{-1}, $\varepsilon(Zr_4(OH)_8^{8+}, ClO_4^-)$ = 3.61 kg·mol^{-1}, $\varepsilon(H^+, ClO_4^-)$ = 0.14 kg·mol^{-1}, $\varepsilon(Zr^{4+}, Cl^-)$ = 0.33 kg·mol^{-1}, and $\varepsilon(H^+, Cl^-)$ = 0.12 kg·mol^{-1}. $\varepsilon(ZrOH^{3+}, Cl^-)$, $\varepsilon(Zr(OH)_2^{2+}, Cl^-)$, $\varepsilon(Zr_3(OH)_9^{3+}, Cl^-)$, and $\varepsilon(Zr_4(OH)_8^{8+}, Cl^-)$, calculated from [20] based on Zr-hydrolysis model, give 0.16, -1.33, 1.04 and -2.62 kg·mol^{-1}, respectively.

In chloride media, the main reaction of zirconium occurring at pH 0-2 is $Zr^{4+} + Cl^- \leftrightarrow ZrCl^{3+}$ with the hydrolysis constant log β^0 = (1.59±0.06) [20].

2.2 Solution analyzes methods

2.2.1 pH measurements

A combined glass pH electrode (pHC3006 Ag/AgCl, radiometer) was used to measure the pH in NaCl and $NaClO_4$ solutions. The pH was adjusted to either 0, 1, 1.5 or 2 by adding Zr free concentrated HCl and $HClO_4$ solutions to 10^{-2} mol·L^{-1} NaCl and $NaClO_4$ solutions, respectively. No significant deviation from the initial pH was observed over time. The pH was constant at ±0.1. For thermodynamic calculations, the measured values were transformed to molal concentrations of protons (pmH$^+$) using the known amount of acid added to a given ionic medium to obtain the selected pH (Table 1).

2.2.2 Solubility measurements

All solution aliquots were ultra-filtered prior to analyses at 5 kDa (Centrisart® I, ultrafiltration unit, Sartorius) in order to exclude the presence of colloidal particles. The aliquots are then acidified in ultra-pure and distilled HNO_3 (0.35 mol·L^{-1}) – HF (0.005 mol·L^{-1}) for inductively coupled plasma mass spectrometry (ICP-MS) analysis. For [Zr] >10^{-9} mol·L^{-1} and pH [0-1], measurements were performed by quadrupole Q-ICP-MS (Xseries 2, THERMOELECTRON) with a quantification limit LQ of 10^{-10} mol·L^{-1}. For lower Zr concentrations (<10^{-9} mol·L^{-1}) and pH [1.5-2], measurements were performed by High Resolution HR-ICP-MS (ELAN 6100, Perkin Elmer) with a LQ of 10^{-11} mol·L^{-1}.

2.2.3 Analytical procedure for quantitative analysis of trace levels of zirconium

In the present study, methods for separation between solid phase and solution are critical. Classical method of filtration is not sufficiently efficient to retain the nanoparticles on the filter. Indeed, depending on the separation yield of nanoparticles/solution, zirconium concentrations can vary up to 1 order of magnitude [12,15]. Therefore, Laser Induced Breakdown Detection (LIBD) technique was used to select the most effective method of nanoparticles/solution separation for measurement of aqueous zirconium. Ultrafiltration system with three pore sizes (5kDa, 10kDa and 20kDa, Sartorius)

and ultracentrifugation device (49,500 g) were used. Ultra-filtrates and supernatant are compared with ultra-pure deionized water (18 MΩ·cm^{-1}, Millipore) free of zirconia particles. For the detection, a pulsed laser beam (10 Hz, λ = 532 nm) generating plasma events (dielectric breakdowns) selectively on particles in liquid media is applied. The energy impulsion was about 10 mJ with a duration of 6 ns. The number of plasma events per number of total laser pulses and their spatial distribution in the laser focus give the colloid concentrations and the size particles. The detection limit is 5 ng·L^{-1} or 10^5 particles·mL^{-1} for 10 nm colloids.

2.2.4 Determination of the surface site number

Method of determination from continuous titration experiments. Suspensions of S/V = 10^6 m^{-1} monoclinic and cubic zirconia equilibrated for several months in 10^{-2} mol·L^{-1} NaCl at pH 0 and 2 were titrated by NaOH solution with Titrino DMS 716 (Metrohm). The pH was measured by a combined glass electrode and recorded with Tiamo software program (Tiamo™1.2. – titration and more). The surface site number (DMSAP, sites per nm²) were calculated using Gran's function [22].

$$DMSAP = \frac{C_{NaOH} \times (V2 - V1) \times N_A}{m \times S \times 10^{18}} \quad \text{(eq.2)}$$

where V1 represents the neutralization volume of the excess proton ions in the suspension by the added hydroxyl ions and V2 the neutralization volume of the excess hydroxyl ions in solution, m is the mass of solid (g), S is the specific surface area (m²/g) and N_A is the Avogadro number.

It should be noted that this function is a mass balance representation of the reactions that take place at the surface of the solid following the interactions of the solid with the solution. It does not represent the real reactions of reaction steps at this interface. The analysis of the variation in function of the added volume gives information on the reactions of the ions added to the suspension (H^+ or OH^-) with the surface of the solid.

Method of determination from crystallographic calculation. The surface site number can be deduced from crystallographic data of zirconia [23,24]. It is determined by dividing the number of zirconium atoms of the surface of zirconia unit cell corresponding to atoms in contact with aqueous solutions, by the area of zirconia unit cell.

2.3 Solid phase characterization methods

Specific surface area (BET). The specific surface area of monoclinic and yttrium stabilized cubic zirconia samples were determined from N_2 adsorption isotherms at 77 K obtained with a Micromeritics ASAP 2010 M. Prior to analyses, the samples were outgassed in vacuum overnight.

X-ray diffractometer (*XRD*). Rigaku MiniFlex600 diffractometer equipped with a copper rotating anode was used to collect XRD patterns of monoclinic and yttrium stabilized cubic zirconia samples.

Data were collected in the 2θ range from 15° to 90° with a step of 0.01° and a scan-speed of 10 °·min^{-1}. The size of crystalline particles was determined from the full width at half maximum (FWHM) of the diffraction peaks based on the Scherrer equation.

Transmission Electron Microscopy (TEM). High-resolution transmission electron microscopy was carried out using a JEOL ARM200F with double Cs-correctors for characterization of the morphology and crystallinity. For imaging, the samples were dispersed in ethanol and deposited on a holey carbon coated grid. The tomography in STEM-HAADF mode (Scanning Transmission Electron Microscopy – High Angle Annular Dark Field) was performed by recording a series of images for a 3D construction. The tomograms were obtained from a 0.13 nm spot size, a current density of 140 pA, an acceleration voltage of 200 kV and a camera with a focal length of 8 cm. The serial acquisition of inclinations (bright field – BF and high-angle annular dark field – HAADF) was carried out using the plug-in of "Digital Micrograph" software, which controls step by step the tilt of the sample, the defocusing and the drift of the sample. The samples were tilted within ± 75° with a 2.5° step. The recorded images are aligned in space by correlating the images consecutively using the IMOD software [25]. The Algebraic Reconstruction Technique (ART) method [26] implemented in the TomoJ plugin [27] of the ImageJ software was used to calculate the reconstructed volumes. Finally, the final volumes were visualized and analyzed using the Slicer software [28].

Small angle x-ray scattering (SAXS). Rigaku Smartalb equipment was used with a rotative copper anticathode. The wavelength of the incident X-ray, λ, was 0.154 nm for Cu Kα radiation. The power of the generator was 9 kW (45mV × 200mA). The q domain was ranged between q=0.04 - 4.2 nm^{-1} or 0.06 - 6 degrees in 2θ, with a step size of 0.02 degree and a rotation rate of 0.53°·min^{-1}. Note that q, which is equal to (4π/λ)sin θ, is the magnitude of the scattering vector.

The samples were loaded into a boron silicate capillary of 0.7 or 1.5 mm of diameter (WJM-Glas Müller GmbH). The direct beam is stopped with a lead beamstop. The diffused intensity was collected by a bi-dimensional D/tex Ultra type detector. In the analysis, the q dependence was attributed to the structure factor, $S(q)$, and the form factor, $P_{\text{sphere}}(q)$, of the spherical particle with the polydispersity of the particle size [29–31]. By introducing the Gaussian distribution ($F(r)$) with the average radius of R of the solid particle and the standard deviation of σ_r, the scattering function $I(q)$ is given by the multiple product of $P_{\text{sphere}}(q)$. The scattering function $I(q)$ is given by:

$$I(q) = n\Delta B^2 P_{\text{sphere}}(q) S(q) \quad \text{(eq.3)}$$

$$P_{\text{sphere}}(q) = \int_0^\infty V^2 \left[\frac{3(\sin qr - qr\cos qr)}{(qr)^3}\right]^2 F(r)dr \quad \text{(eq.4)}$$

$$F(r) = \exp\left[\frac{-(r-R)^2}{2\sigma_r^2}\right] / \int_0^\infty \exp\left[\frac{-(r-R)^2}{2\sigma_r^2}\right] dr \quad \text{(eq.5)}$$

where n, ΔB^2, and V are the number of particles per unit volume in the solution, the scattering contrast difference between the particle and solution, and the volume of single particle, respectively. The experimental SAXS profiles in the range of 0.07 nm^{-1} <q <1.0 nm^{-1} were analyzed in the least-square fitting analysis based on the above equations to determine the average size of solid phase particle (R), its standard deviation (σ_r) and constant A = $n\Delta B^2V^2S(q)$.

3 Results and Discussion

3.1 Morphological characterization

A detailed morphological and structural analysis of zirconia samples before and after alteration experiments were performed using XRD, HR-TEM, STEM-HAADF and SAXS.

Figure 2 shows XRD patterns of raw zirconia before alteration experiments confirming the monoclinic MZ and cubic YSZ crystallographic structures. The crystallite size determined by Scherrer equation gives values close to 28 nm for MZ and 6 nm for YSZ. Raw monoclinic zirconia was also characterized by HR-TEM showing very well crystallized particles without any amorphous phase (Figure 3-a). STEM-HAADF characterization reveals the presence of agglomerates of nanoparticles with a size particle of (28±5) nm similar to the crystallite size (Figure 4-a). In addition, the reconstruction in 3D of the aggregates of nanoparticles from the alignment of two series of BF and HAADF provides an overview of the morphology and the surface state of nanoparticles. Figure 4-b and Figure 4-c show the typical images extracted from the series of inclinations for the shape of MZ aggregates in equilibrium with a pH 1 aqueous solution in HCl and $HClO_4$ media, respectively. These samples were chosen for their high reactivity (low S/V ratio 10^6 m^{-1}) among all the series of experiments. After more than 12 months of dissolution, MZ particles size in HCl and $HClO_4$ is not modified and is within the range of the measurement errors: (26±2) nm in HCl media and (32±4) nm in $HClO_4$ media (Figure 3-b-c). The 3D reconstruction visualization and HR-TEM show that the morphology and the structure of nanoparticles in the raw state and after reaching equilibrium in acidic media are similar without any evolution of the interfacial morphology observed during dissolution. The characterization on raw and altered YSZ nanoparticles was conducted by HR-TEM. The in-depth analysis shows well-oriented atomic planes in raw sample (Figure 3), confirming the strong tendency to agglomerate. The size distribution of raw YSZ nanoparticles gives (7±2) nm in agreement with the crystallite size determined by XRD. After alteration in acidic HCl and $HClO_4$ media at pH 0, the nanoparticles size remains stable within given uncertainties at (8±2) nm.

The micro-characterization using various techniques showed that all the alteration experiments were conducted in presence of nanoparticles close to agglomerates of crystallites. At very low pH and high surface reactivity, no modification of the morphology was observed, as well as the absence of the

formation of amorphous phase for both structures. Nevertheless, heterogeneous areas are observed at the border of some nanoparticles (Figure S4 in supplementary data). These may be attributed to the modification of atomic plans following the dissolution process of the nanoparticles. However, the occurrence of such modification was rarely observed.

To deepen the micro-characterization of the solids, the particle size before, during and at equilibrium was determined by SAXS. The results in Figure 5 present the characteristic point on monoclinic ZrO_2 samples obtained at $q \approx 0.2$ nm^{-1} corresponding to the gyration radius (R_g) of the Guinier regime. The average particle size of monoclinic ZrO_2 before contact with an aqueous solution was determined to be (32±6) nm from the least-square fitting analysis of the SAXS profiles based on eq. (3)-(5). This value is coherent with the values determined by XRD and TEM. After contacting aqueous solutions at pH 2, the MZ particle size was determined to be (34±7) nm, which is almost the same as that before contact with aqueous solution. The result shows the weak modification of the particle size even after reaction in acidic media for 74 days. On the other hand, the particle size at pH 0 was determined to be (21±4) nm after 171 days of contact with aqueous solution, slightly smaller than that of before contact. For wave vector values below 0.2 nm^{-1}, intensity $I(q)$ keeps increasing with the decrease of q. For the lowest values of q, a zero slope is not observed for most spectra. This means that, in addition to the presence of individual particles, the particles form aggregates larger than 90 nm, calculated from the limit of the q interval (0.07 nm^{-1} < q). For cubic ZrO_2 samples, particle size before contact with an aqueous solution is (12±2) nm determined from the characteristic point at $q \approx 0.6$ nm^{-1}, which is slightly higher than the values obtained by XRD and TEM. After contacting with solution (86 days at pH2 and 62 days at pH0), the size of particles are within the range 8-12 nm almost independent of aqueous solution conditions, indicating a slight modification of the particle size after reaction in acidic media. For wave vector values below 0.6 nm^{-1}, the intensity $I(q)$ continues to increase with the decrease of q. This means that the particles form aggregates are larger than 90 nm, calculated from the limit of the q interval (0.07 nm^{-1} < q). Finally, the SAXS spectra analysis results for both monoclinic and cubic phase show that the mean nanoparticle sizes under the different conditions studied (pH 0 and 2, HCl and $HClO_4$ media) are comparable before and during dissolution experiments, indicating that the dissolution process of ZrO_2 did not induce precipitation or the formation of a new solid phase in the sample.

3.2 Assessment of the ultrafiltration efficiency

The ultrafiltration efficiency was assessed using laser induced breakdown detection (LIBD) by measuring the breakdown probability (or the number of plasma events) on ultrafiltered solutions and supernatant (ultracentrifugation) as function of increasing pulse energy.

Figure 6-a compares the LIBD s–curves obtained by the ultrafiltration and the ultracentrifugation of monoclinic zirconia nanoparticles. The LIBD s–curve of blank solution (without zirconia nanoparticles) exhibits a low pulse energy threshold at 44 µJ corresponding to the presence of trace levels of impurities. As the ultrafilter pore size increases (5kDa, 10 kDa and 20 kDa), the threshold in the s–curves at 5 kDa and 10 kDa does not significantly differ from the blank solution. Thus, the ultrafiltered solutions at 5 kDa and 10 kDa could be considered to be free of nanoparticles. For the ultrafilter pore size of 20 kDa, the threshold shifts to lower pulse energies (38 µJ) implying the presence of nanoparticles of ZrO_2: the lower is the threshold of the pulse energy, the higher is the probability of presence of nanoparticles in solution. This observation is confirmed with the last s–curves obtained from ultracentrifugation separation method with the lowest threshold pulse energies at 12 µJ (Figure 6–b). Therefore, the results were compared from ultrafiltered solution at 5 kDa in contact with monoclinic zirconia at various pH. The LIBD s–curves give similar results to that of blank solution. The absence of nanoparticles in the ultrafiltered solution is precious information, any Zr analyzed in this solution by ICP–MS is by consequence in non-colloidal form allowing the application of aqueous speciation models for solubility determination. Indeed, working with nanoparticles required efficient and high-performance separation device to separate them from solution. The typical filtration methods such as 0.22µm or 0.45µm filter membranes failed when working with nanoparticles. The optimization of a suitable method of filtration allows decreasing the uncertainties of the measurement, avoiding pitfalls reported in literature confirming the influence of colloids and solid form on the solubility values.

To gain insight into the degree of zirconium losses during ultrafiltration process, the adsorption of Zr on the filter was studied. Zirconium adsorption tests were conducted on the 5 kDa ultrafilters. Standard zirconium solutions were prepared at pH 0, 1 and 2 (I = 0.01) and ultrafiltered for analysis by Q-ICP-MS. For each standard solution, the total concentration of Zr(IV) was measured before and after ultrafiltration, and the mean amounts of zirconium retention/adsorption as a function of initial concentrations of standard solutions are shown in Figure 7. The amount of adsorbed zirconium is constant in the [0-2] pH range: (13.7±0.3)% of dissolved zirconium is adsorbed on ultrafiltration membrane. The concentration values given in the present work are corrected from the adsorption coefficient.

3.3 Solubility data

Concentrations of Zr were followed by periodic sampling of aliquots over more than one year. Figure 8 displays [Zr] as function of S/V×time (S/V×t) (for more details see in supplementary information Figures S1 and S2). The experimental data show that long times and large S/V ratios both favor approach of equilibrium. For almost all experimental conditions, equilibrium is reached except for

YSZ at pH0 in (Na,H)Cl showing a continuous dissolution after 466 days of contact. Table 2 reports the detailed values of solubility data, also shown in Figure 1. This work provided new solubility values, in particular at pH [1.5-2] for monoclinic phase (~$2x10^{-10}$ mol·l^{-1}). These low values are explained by the efficient ultrafiltration method to remove colloids and the use of HR-ICP-MS to decrease the quantification limit. For further thermodynamic treatment, we used only data at high (S/V×t) to determine the equilibrium concentrations.

An average fraction of surface sites involved in the dissolution process was determined relating the measured element concentration in solution to the number of crystallographic surface sites per solution volume. Without considering the potential dominance of individual crystal planes in surface/solution exchange, the total number of moles at the surface per solution volume may be estimated from the crystallographic site density (in sites·nm^{-2}), the specific surface area ((36.2±0.1) $m^2 \cdot g^{-1}$ for MZ and (139.4±0.5) $m^2 \cdot g^{-1}$ for YSZ) and the mass/solution volume ratio. The crystallographic site density obtained for MZ and YSZ are 7.5 and 7.6 sites.nm^{-2}, respectively. Compared to these results, experimental protonable surface site density was obtained for the higher S/V ratio (10^6 m^{-1}) by acid-base titration at pH 0 and 2 (Table 3). For this S/V ratio, the number of dissolved monolayers was determined at pH 0 (after 383 days of MZ alteration and 466 days of YSZ alteration) and pH 2 (after reaching the equilibrium). The results show that the mass of Zr dissolved to reach the observed solubility equilibrium of ZrO_2 corresponds to the dissolution of much less than 1 monolayer. These results are consistent with a previous study performed onto monoclinic and yttrium stabilized tetragonal ZrO_2 [32] and confirm the strong refractory character of the solids.

3.4 Solubility constants and Zr speciation

The Zr speciation in solution both for monoclinic and cubic phases was determined using the Thermochemical Database of Nuclear Energy Agency NEA-TDB from Brown et al. [20], and taking into account the strong effect of ionic strength on solubility at low pH values, and the hydrolysis and SIT models. Polymer and monomer hydrolysis species distribution as well as chloride complexes were determined for 10^{-2} mol·L^{-1} (Na,H)Cl and (Na,H)ClO_4 solution in pH 0-2. In chloride and perchloride media at pH range [0-2] the main species exist under Zr^{4+}, $ZrOH^{3+}$, $Zr(OH)_2^{2+}$and $Zr(OH)_4$ forms. Mainly monomer hydrolysis species are obtained. Dissolved polymer hydrolysis species ($Zr_3(OH)_9^{3+}$, $Zr_4(OH)_8^{8+}$) are formed at very low pH and for high Zr-concentration in solution in presence of cubic zirconia. Chloride complex ($ZrCl^{3+}$) is formed at very low pH. Detailed predominance of aqueous Zr solution species are displayed in supplementary data Figure S3.

Thus, based on the Zr-hydrolysis and SIT models [20] for aqueous speciation of dissolved zirconium and using the solubility constant K_s^0 as only fit variable, experimental solubility data are compared

with thermodynamic model data (Figure 9, Table 2). The solubility constants log K_s^0 were calculated considering either the monoclinic or the cubic ZrO_2 solid phase limiting the solubility. The obtained log K_s^0 (298 K) value for the monoclinic phase (-7.33±0.69) is lower than the value derived by Brown et al. (-7.0±1.6) as well as the uncertainty values associated [20]. Brown et al. explained the high uncertainty by the selection of solubility data from crystallized solid to amorphous hydroxides. This work has strengthened the thermodynamic data for well-crystallized solids. Our characterizations clearly show that the solid remains crystallized even after more than 1 year of contact with solution. For the cubic phase, a log K_s^0 (298 K) value of (-5.86±0.35) is obtained, higher than the value obtained with the monoclinic phase. The obtained solubility constants of the nanoparticles are independent on the ionic medium within the experimental uncertainties as expected. Solubility data are obtained from ZrO_2 nanoparticles, and to account for the effect of particle size, solubility constants have been re-evaluated using the Schindler equation (eq. 6) [33,34]:

$$\ln K_s^0 = \ln K_s^0\left(\overline{S}_{=0}\right) + \frac{2\overline{\gamma}}{3RT}\overline{S} \qquad \text{(eq.6)}$$

with $K_s^0\left(\overline{S}_{=0}\right)$ solubility constant (I=0) related to the particle size effect, $\overline{\gamma}$ the surface energy of nanoparticles (J·m^{-2}), and $\overline{S}$ the molar surface ($\overline{S}_{\mathrm{monoclinic}}$ = 3302 m²·mol^{-1}, $\overline{S}_{\mathrm{cubic}}$ = 12717 m²·mol^{-1}).

This relation shows that the effect of particle size is the key parameter dominating the dissolution of particles with size below 100 nm [5,34–37]. Kobayashi et al. demonstrate the effect of particle size on ZrO_2 solubility: solubility decreases with increasing particle size and crystalline degree of the solid (as opposed to amorphous and hydroxide phases) [5]. Using the surface energy for the hydrous monoclinic phase (2.86±0.31) J·m^{-2} [38] and for the hydrous cubic phase (0.85±0.07) J·m^{-2} [39], the solubility constant for large crystals log $K_s^0\left(\overline{S}_{=0}\right)$ was calculated as (-8.43±0.69) for monoclinic phase and (-7.12±0.35) for cubic phase. By this approach, the discrepancy in solubility constant values has been reduced.

3.5 Possible effect of Y-release on Zr-solubility values?

In dissolution experiments with YSZ cubic phase, strong release of yttrium has been observed at all studied pH values despite very low release of Zr. The Y release after 69 days corresponds to the release of (53±8)% of the Y inventory of the YSZ particles indicating a fast release of Y in solution, independent on the media composition. Yttrium release from YSZ is reported in the literature [40] for pH values <4. At acidic pH, the solubility of Y is high [41,42] while it decreases at neutral pH [42]. The release of large quantities of Y to a depth of few nanometers implies that hydrolysis of YSZ bonds occurs accompanied by diffusion of H_2O into the crystal lattice. Geochemical modelling (PHREEQC) of a solid solution of La_2O_3 (homologue to Y) has shown that this composition of a solid solution of REE

and ZrO_2 is not stable under acid conditions and release of a large fraction (more than 99.9%) of its content of REE is expected upon equilibrating with the aqueous solution. The question is if the cubic crystal structure in the leached surface region remains cubic after the release of its Y content. Leaching studies of a mixed cubic and monoclinic $Zr_{0.9}Nd_{0.1}O_{1.95}$ phase [43] have shown that the crystal structure remains mixed cubic and monoclinic. This indicates that the cubic structure may have been conserved in our experiments. On the other hand, the authors did not use a surface-sensitive XRD technique and it cannot be excluded that the surface region has been transformed crystallographically. Our HR-TEM study clearly shows well-crystallized nanoparticles, without new precipitates or amorphous phase, indicating that the cubic structure may have remained stable.

Zr concentrations in solution measured in the present study are much higher than that observed in our experiments for the monoclinic phase. This increase of the solubility constant cannot be explained by the presence of yttrium since Y has been leached from the surface region. However, the substitution of Zr by Y for stabilizing the cubic phase leads to the creation of O^{2-} vacancy sites increasing the ionic character of Zr-O bonds and the dissolution effect [44,45]. The reactivity of the vacancy site type regarding to water was assessed by Kossoy et al. on undoped and Gd-doped cerium oxides in which the authors characterized by XPS that hydroxyl ions are strongly bound to oxygen vacancy sites by water dissociation [46]. They also showed that this phenomenon occurs only at the surface and does not involve the bulk. Moreover, in our previous study conducted on the solubility of tetragonal zirconia [32], XPS characterizations were performed and revealed that hydroxyl ions are dominant in the tetragonal phase of ZrO_2 compared to the monoclinic phase (Figure S5 in supplementary data). Therefore, simultaneous reactions at surface with the enrichment in water molecules bond to oxygen vacancy sites and the leaching of yttrium may have changed the surface energy and may have created a more open surface structure with a reduction of the average coordination number of surface Zr atoms, leading to an easiest detachment of surface Zr atoms. Therefore, the surface energy values taken from literature may not be applicable as surface energy measurements are taken in neutral water, less prone to removal of Zr. Measurement of surface energy of leached YSZ particles under acid conditions should be performed to study this hypothesis.

4 Conclusion

The present study aimed to determine the solubility of well crystallized nanoparticles of zirconia in acidic media for two crystallographic structures: monoclinic and yttrium stabilized cubic. Its high chemical stability required the development of reliable and robust analytical method to improve the detection and the quantification of zirconium at ultra-trace level. Our experimental approach has

allowed reducing the uncertainties. This was the condition of being able to distinguish clearly for the first time between the solubility of monoclinic and Y stabilized cubic ZrO_2.

A consistent set of solubility constants derived from this work and that of Brown et al. [20] for monoclinic and cubic ZrO_2 was obtained, indicating that nanoparticles can be used for solubility assessment if extremely low quantification limits are assured and solution are carefully ultrafiltered. Taking into account the ionic strength, the effect of particle size and the surface energies, the solubility constant of large crystals $\log\ \mathrm{K}_{\mathrm{s}}^{0}\left(\overline{S}_{=0}\right)$ was calculated to (-8.43±0.69) for the monoclinic structure and (-7.12±0.35) for the cubic structure. However, in the calculation of the solubility constant, the surface energy values were taken here from literature but no account could be taken for the effect of the release of Y on surface energy of the cubic phase, in particular in acidic media promoting Y and Zr release. As a perspective, the surface energies needs to be determined experimentally under the same experimental conditions as those of the solubility studies.

5 Acknowledgement

We gratefully thank the two anonymous reviewers for their careful reading of the manuscript and their many helpful comments and suggestions that helped to clarify the content of the paper. We would also like to express our deep acknowledge to Pr. X. Gaona (KIT) and Dr. S. Szenknect (ICSM) for fruitful discussions, and to Dr. K. David (SUBATECH) for low Zr-concentration measurements by HR-ICP-MS and advices for Zr-measurement by Q-ICP-MS. We are also very grateful to Pr. O. Ersen (IPCMS) and the national network METSA for giving the opportunity to perform STEM-HAADF measurements. Finally, we kindly thank Mr. E. Chevrel (DSEE) for BET measurements, and Mr. Z. Yan (SUBATECH) for the titration experiments.

6 References

[1] G. Bertrand, R. Mévrel, Zirconia coatings realized by microwave plasma-enhanced chemical vapordeposition, Thin Solid Films. 292 (1997) 241–246. doi:10.1016/S0040-6090(96)09099-2.

[2] P. Blanchart, Extraction, Properties and Applications of Zirconia, in: Ind. Chem. Oxides Emerg. Appl., John Wiley & Sons Ltd, Chichester, UK, 2018: pp. 165–209. doi:10.1002/9781119424079.ch4.

[3] V. Kalavathi, R. Kumar Bhuyan, A detailed study on zirconium and its applications in manufacturing process with combinations of other metals, oxides and alloys – A review, Mater. Today Proc. 19 (2019) 781–786. doi:10.1016/j.matpr.2019.08.130.

[4] A.T. Motta, A. Couet, R.J. Comstock, Corrosion of Zirconium Alloys Used for Nuclear Fuel

457 Cladding, Annu. Rev. Mater. Res. 45 (2015) 311–343. doi:10.1146/annurev-matsci-070214-
458 020951.

459 [5] T. Kobayashi, D. Bach, M. Altmaier, T. Sasaki, H. Moriyama, Effect of temperature on the
460 solubility and solid phase stability of zirconium hydroxide, Radiochim. Acta. 101 (2013) 645–
461 651. doi:10.1524/ract.2013.2074.

462 [6] M. Rand, J. Fuger, I. Grenthe, V. Nech, D. Rai, Chemical Thermodynamics of thorium volume
463 11, OECD Publishing, 2008. doi:10.1017/CBO9781107415324.004.

464 [7] R. Guillaumont, T. Fanghanel, J. Fuger, I. Grenthe, V. Neck, D.A. Palmer, M.H. Rand, Update on
465 the Chemical Thermodynamics of U, Np, Pu, Am and Tc, NEA-OECD, Elsevier, Palaiseau,
466 France, 2003.

467 [8] C. Ekberg, G. Kallvenius, Y. Albinsson, P.L. Brown, Studies on the Hydrolytic Behavior of
468 Zirconium(IV), J. Solution Chem. 33 (2004) 47–79.
469 http://dx.doi.org/10.1023/B:JOSL.0000026645.41309.d3.

470 [9] H. Bilinski, M. Branica, L.G. Sillen, Precipitation and hydrolysis of metallic ions. II. Studies on
471 the solubility of zirconium hydroxide in dilute solutions and in 1 M NaClO4, Acta Chem. Scand.
472 Divid. into Acta Chem. Scand., Ser. A Ser. B; Vol 20. (1966) Pages: 853-61.

473 [10] H.-R. Cho, C. Walther, J. Rothe, V. Neck, M.A. Denecke, K. Dardenne, T. Fanghänel, Combined
474 LIBD and XAFS investigation of the formation and structure of Zr(IV) colloids, Anal. Bioanal.
475 Chem. 383 (2005) 28–40. doi:10.1007/s00216-005-3354-6.

476 [11] E. Curti, C. Degueldre, Solubility and hydrolysis of Zr oxides: a review and supplemental data,
477 Radiochim. Acta. 90 (2002) 801–804. doi:10.1524/ract.2002.90.9-11_2002.801.

478 [12] T. Kobayashi, T. Sasaki, I. Takagi, H. Moriyama, Solubility of zirconium(IV) hydrous oxides, J.
479 Nucl. Sci. Technol. 44 (2007) 90–94. doi:10.1080/18811248.2007.9711260.

480 [13] P.N. Kovalenko, K.N. Bagdasarov, Determination of zirconium hydroxide dissoltuion rate, Zhur.
481 Neorg. Khim. 6 (1961) Pages: 534-538.

482 [14] M.A. Pouchon, E. Curti, C. Degueldre, L. Tobler, The influence of carbonate complexes on the
483 solubility of zirconia: new experimental data, Prog. Nucl. Energy. 38 (2001) 443–446.
484 doi:10.1016/S0149-1970(00)00155-4.

485 [15] T. Sasaki, T. Kobayashi, I. Takagi, H. Moriyama, Solubility measurement of zirconium(IV)
486 hydrous oxide, Radiochim. Acta. 94 (2006) 489–494. doi:10.1524/ract.2006.94.9-11.489.

487 [16] I.A. Sheka, T. V Pevzner, Solubility of zirconium and hafnium hydroxides in sodium hydroxide

488 solutions, Russ. J. Inorg. Chem. 5 (1960) 1119–1121.

489 [17] A. Veyland, Propriétés thermodynamiques, cinétiques et structurales de complexes simples et
490 mixtes du zirconium(IV) avec les ions hydroxyle et carbonate, Thesis, Univ. of Reims
491 Champagne-Ardenne, 1999.

492 [18] N. Michel, Étude de la solubilité des oxydes et oxohydroxydes de zirconium caractérisés :
493 effets des propriétés du solide et de sa surface, Http://Www.Theses.Fr. (2005).

494 [19] M. Altmaier, V. Neck, T. Fanghänel, Solubility and colloid formation of Th(IV) in concentrated
495 NaCl and MgCl2 solution, Radiochim. Acta. 92 (2004) 537–543.
496 doi:10.1524/ract.92.9.537.54983.

497 [20] P. Brown, E. Curti, B. Grambow, Chemical thermodynamics of zirconium volume 8, OECD
498 Publishing, 2005.

499 [21] C. Hellwig, M. Pouchon, R. Restani, F. Ingold, G. Bart, Fabrication and microstructure
500 characterization of inert matrix fuel based on yttria stabilized zirconia, J. Nucl. Mater. 340
501 (2005) 163–170.

502 [22] G. Gran, Determination of the equivalence point in potentiometric titrations. Part II, Analyst.
503 77 (1952) 661. doi:10.1039/an9527700661.

504 [23] S.P. Terblanche, Thermal-expansion coefficients of yttria-stabilized cubic zirconias, J. Appl.
505 Crystallogr. 22 (1989) 283–284. doi:10.1107/S0021889888013937.

506 [24] C.J. Howard, R.J. Hill, B.E. Reichert, Structures of ZrO 2 polymorphs at room temperature by
507 high-resolution neutron powder diffraction, Acta Crystallogr. Sect. B Struct. Sci. 44 (1988)
508 116–120. doi:10.1107/S0108768187010279.

509 [25] D.N. Mastronarde, Dual-Axis Tomography: An Approach with Alignment Methods That
510 Preserve Resolution, J. Struct. Biol. 120 (1997) 343–352. doi:10.1006/jsbi.1997.3919.

511 [26] R. Gordon, R. Bender, G.T. Herman, Algebraic Reconstruction Techniques (ART) for three-
512 dimensional electron microscopy and X-ray photography, J. Theor. Biol. 29 (1970) 471–481.
513 doi:10.1016/0022-5193(70)90109-8.

514 [27] C. MessaoudiI, T. Boudier, C. Sorzano, S. Marco, TomoJ: tomography software for three-
515 dimensional reconstruction in transmission electron microscopy, BMC Bioinformatics. 8
516 (2007) 288. doi:10.1186/1471-2105-8-288.

517 [28] A. Fedorov, R. Beichel, J. Kalpathy-Cramer, J. Finet, J.-C. Fillion-Robin, S. Pujol, C. Bauer, D.
518 Jennings, F. Fennessy, M. Sonka, J. Buatti, S. Aylward, J. V Miller, S. Pieper, R. Kikinis, 3D Slicer

519 as an image computing platform for the Quantitative Imaging Network, Magn. Reson.
520 Imaging. 30 (2012) 1323–1341. doi:10.1016/j.mri.2012.05.001.

521 [29] R. Motokawa, T. Taniguchi, Y. Sasaki, Y. Enomoto, F. Murakami, M. Kasuya, M. Kohri, T.
522 Nakahira, Small-angle neutron scattering study on specific polymerization loci induced by
523 copolymerization of polymerizable surfactant and styrene during miniemulsion
524 polymerization, Macromolecules. 45 (2012) 9435–9444. doi:10.1021/ma301776b.

525 [30] J. S. Higgins; H. C. Benoit, Polymers and neutron scattering, in: Polym. Int., Clarendon Press,
526 1995: p. 436.

527 [31] R.-J. Doe, Methods of Neutron and X-ray Scattering in Polymer Science, Oxford University
528 Press, 2000.

529 [32] B. Grambow, J. Vandenborre, T. Suzuki-Muresan, V. Philippini, A. Abdelouas, P. Deniard, S.
530 Jobic, Solubility equilibrium and surface reactivity at solid/liquid interfaces of relevance to
531 disposal of nuclear waste, J. Chem. Thermodyn. 114 (2017) 172–181.
532 doi:10.1016/j.jct.2017.05.038.

533 [33] Schindler, Equilibrium Concepts in Natural Water Systems, American Chemical Society,
534 WASHINGTON, D.C., 1967. doi:10.1021/ba-1967-0067.

535 [34] A.E. Nielsen, O. Söhnel, Interfacial tensions electrolyte crystal-aqueous solution, from
536 nucleation data, J. Cryst. Growth. 11 (1971) 233–242. doi:10.1016/0022-0248(71)90090-X.

537 [35] T. Bundschuh, R. Knopp, R. Müller, J.I. Kim, V. Neck, T. Fanghänel, Application of LIBD to the
538 determination of the solubility product of thorium(IV)-colloids, Radiochim. Acta. 88 (2000)
539 625–629.

540 [36] P. Aharon, Geochemistry of sedimentary carbonates, Geochim. Cosmochim. Acta. 57 (1993)
541 2919–2920. doi:10.1016/0016-7037(93)90401-H.

542 [37] J.W. Morse, F.T. Mackenzie, Geochemistry of sedimentary carbonates, Geochemistry
543 Sediment. Carbonates. (1990) 707. doi:10.1016/0016-7037(93)90401-h.

544 [38] A. V. Radha, O. Bomati-Miguel, S. V. Ushakov, A. Navrotsky, P. Tartaj, Surface enthalpy,
545 enthalpy of water adsorption, and phase stability in nanocrystalline monoclinic zirconia, J. Am.
546 Ceram. Soc. 92 (2009) 133–140. doi:10.1111/j.1551-2916.2008.02796.x.

547 [39] G.C.C. Costa, S. V. Ushakov, R.H.R. Castro, A. Navrotsky, R. Muccillo, Calorimetric
548 Measurement of Surface and Interface Enthalpies of Yttria-Stabilized Zirconia (YSZ), Chem.
549 Mater. 22 (2010) 2937–2945. doi:10.1021/cm100255u.

[40] J.B. Rosenholm, F. Manelius, H. Fagerholm, L. Grönroos, H. Byman-Fagerholm, Surface and bulk properties of yttrium stabilized ZrO2 powders in dispersions, in: R.H. Ottewill, A.R. Rennie (Eds.), Trends Colloid Interface Sci. VIII, Steinkopff, Darmstadt, 1994: pp. 51–58.

[41] M. Yoshimura, T. Noma, K. Kawabata, S. Sōmiya, Role of H2O on the degradation process of Y-TZP, J. Mater. Sci. Lett. 6 (1987) 465–467. doi:10.1007/BF01756800.

[42] M. Yoshimura, T. Hiuga, S. Somiya, Dissolution and Reaction of Yttria-Stabilized Zirconia Single Crystals in Hydrothermal Solutions, J. Am. Ceram. Soc. 69 (1986) 583–584. doi:10.1111/j.1151-2916.1986.tb04798.x.

[43] Y. Ding, H. Dan, X. Lu, X. Shu, Z. Hong, S. Zhang, Phase evolution and chemical durability of Zr1-xNd xO2-x/2 (0 ≤ x ≤ 1) ceramics, J. Eur. Ceram. Soc. 37 (2017) 2673–2678. doi:10.1016/j.jeurceramsoc.2017.02.053.

[44] A. Christensen, E.A. Carter, First-principles study of the surfaces of zirconia, Phys. Rev. B. 58 (1998) 8050–8064. doi:10.1103/PhysRevB.58.8050.

[45] M.W. Finnis, A.T. Paxton, M. Methfessel, M. Van Schilfgaarde, Crystal structures of zirconia from first principles and self-consistent tight binding, Phys. Rev. Lett. 81 (1998) 5149–5152. doi:10.1103/PhysRevLett.81.5149.

[46] A. Kossoy, H. Cohen, T. Bendikov, E. Wachtel, I. Lubomirsky, Water adsorption at the surface of pure and Gd-doped ceria, Solid State Ionics. 194 (2011) 1–4. doi:https://doi.org/10.1016/j.ssi.2011.05.011.

List of Figures

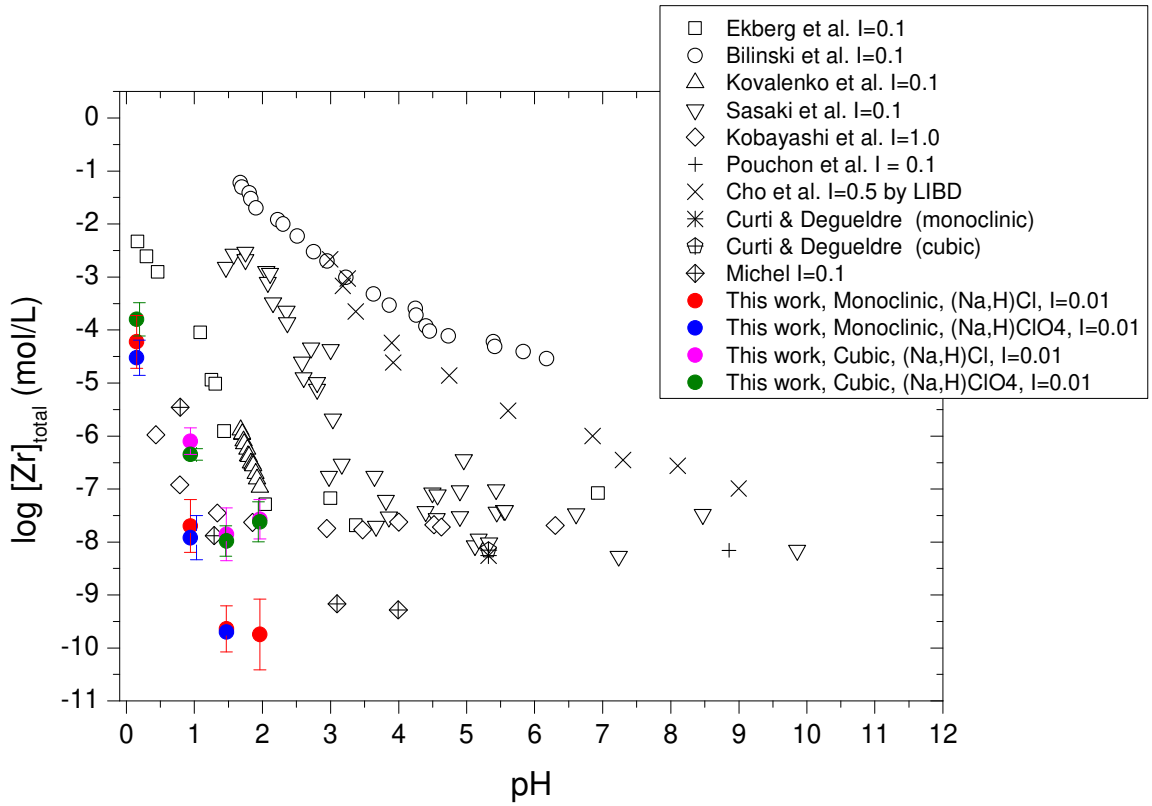

597

598 Figure 1: $\log[Zr]_{total}$ ($mol \cdot L^{-1}$) as function of pH and ionic force obtained in our work compared to data

599 sets of literature [8,9,18,10–17].

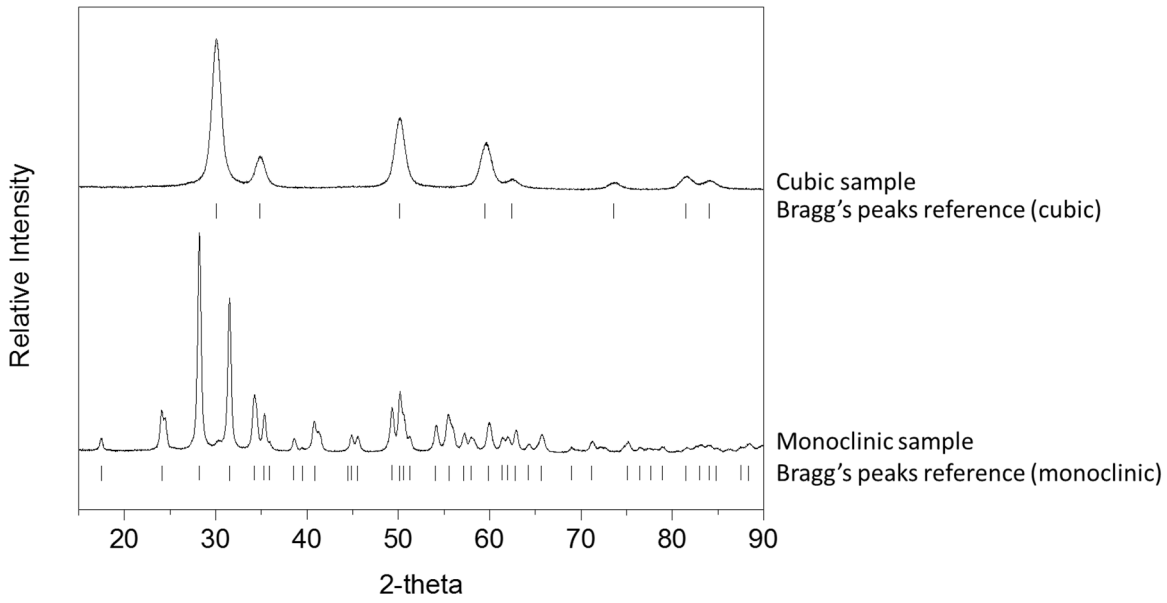

600

601 Figure 2: XRD patterns of monoclinic and cubic ZrO_2.

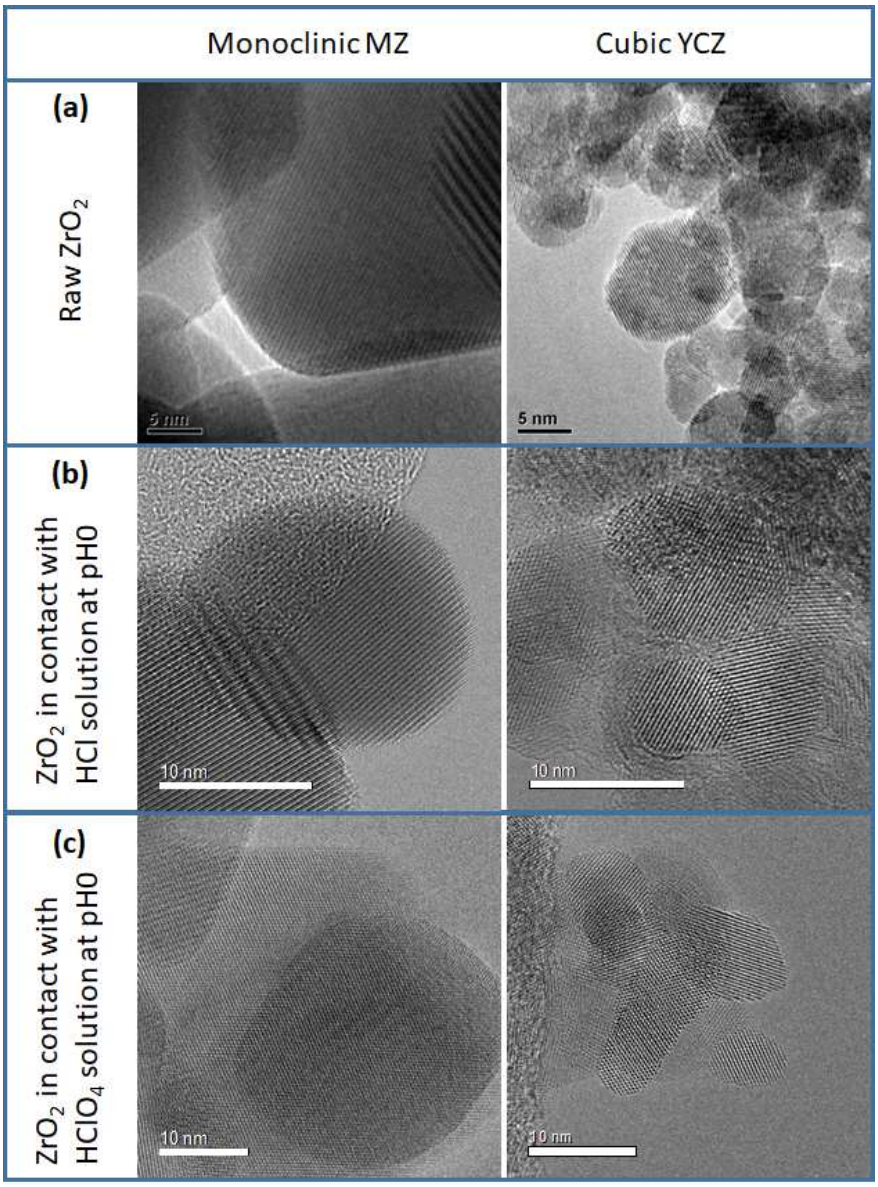

602

603 Figure 3: HR-TEM pictures of monoclinic and cubic zirconia: (a) before contacting with aqueous
604 solutions, in contact with (b) HCl and (c) $HClO_4$ solutions at pH0.

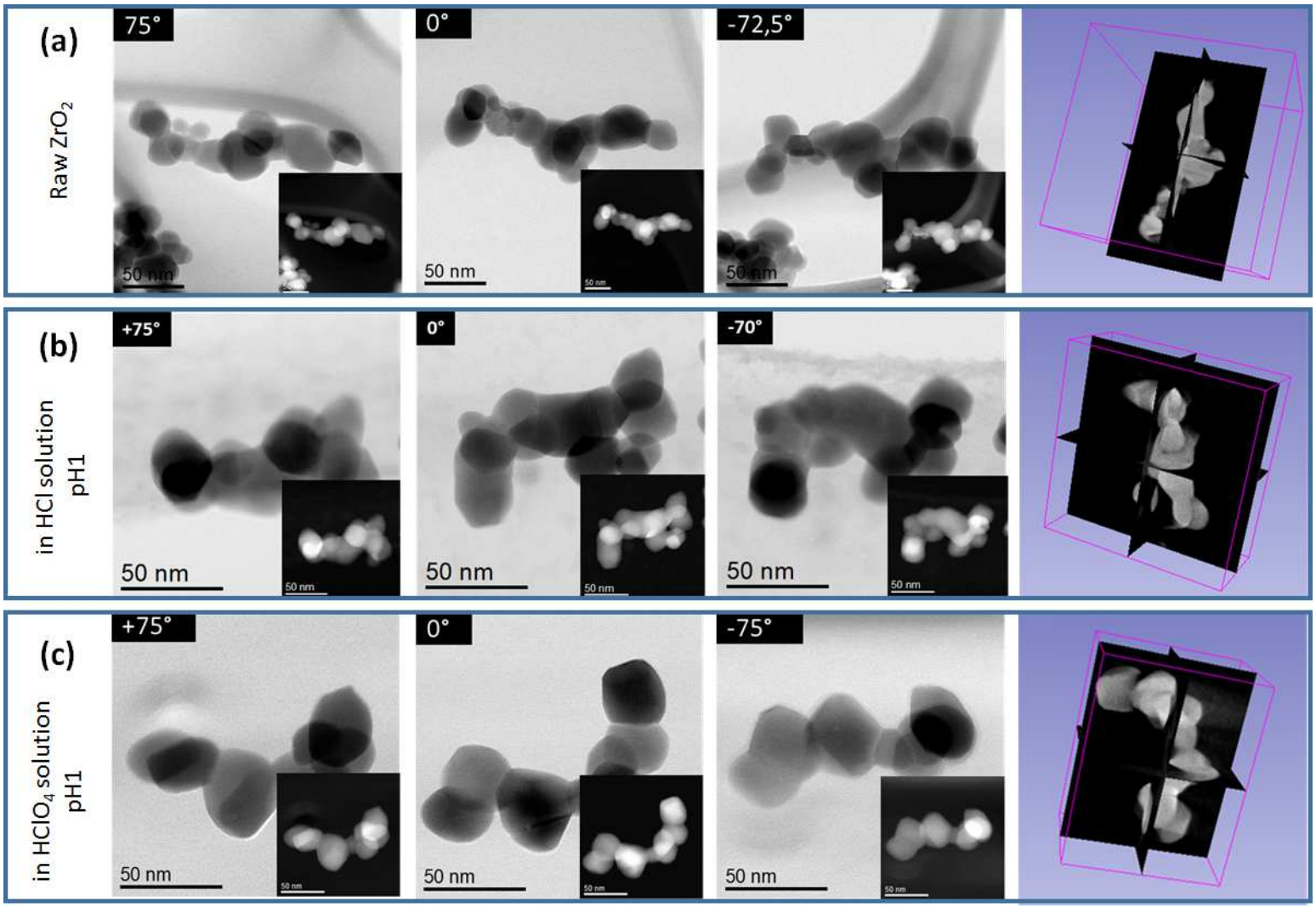

Figure 4: Typical TEM images extracted from the series of inclinations used for the 3D reconstruction of a raw monoclinic ZrO_2 aggregate, altered in HCl and $HClO_4$ medium at pH1 after more than 12 months.

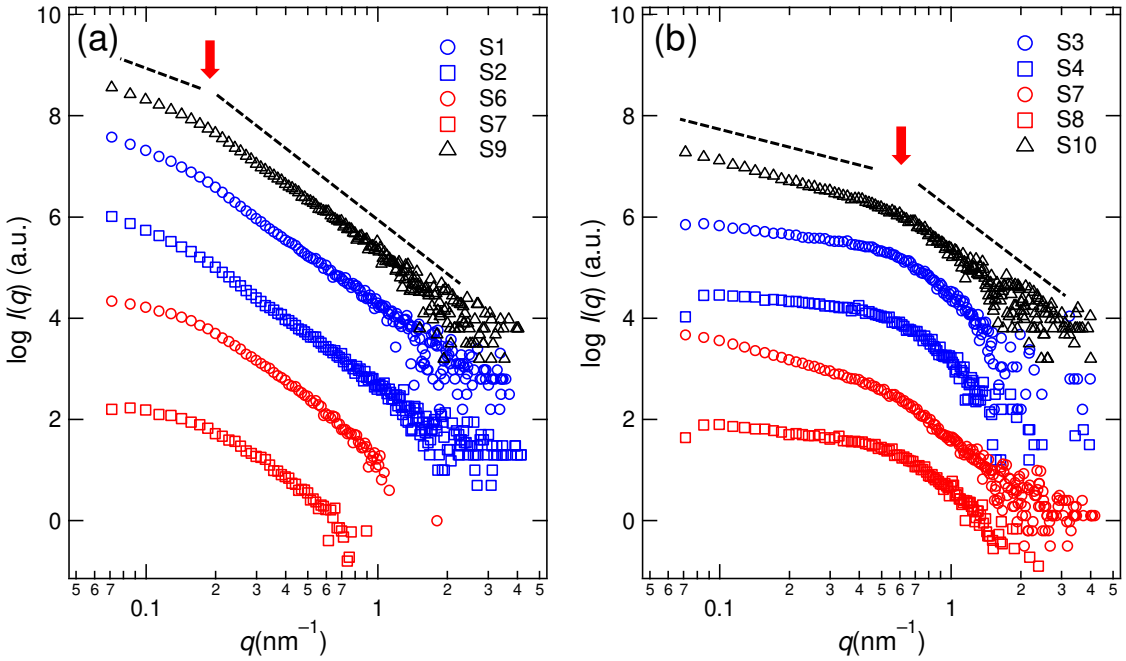

608

609 Figure 5: Simplified representation of SAXS spectra of ZrO_2 samples a) monoclinic and b) cubic. The
610 spectra have been shifted vertically to avoid overlap when processing the spectra. Monoclinic MZ: at
611 pH2, 74 days of contact (S1) NaCl 0.01M / HCl, (S2) $NaClO_4$ 0.01M / $HClO_4$; at pH 0, 171 days of
612 contact (S5) NaClO4 0.01M / $HClO_4$, (S6) NaCl 0.01M / HCl; (S9) raw MZ sample before alteration.
613 Cubic YSZ: at pH2, 86 days of contact (S3) $NaClO_4$ 0.01M / $HClO_4$, (S4) NaCl 0.01M / HCl; at pH0, 62
614 days of contact (S7) $NaClO_4$ 0.01M / $HClO_4$, (S8) NaCl 0.01M / HCl pH0; (S10) raw YSZ sample before
615 alteration.

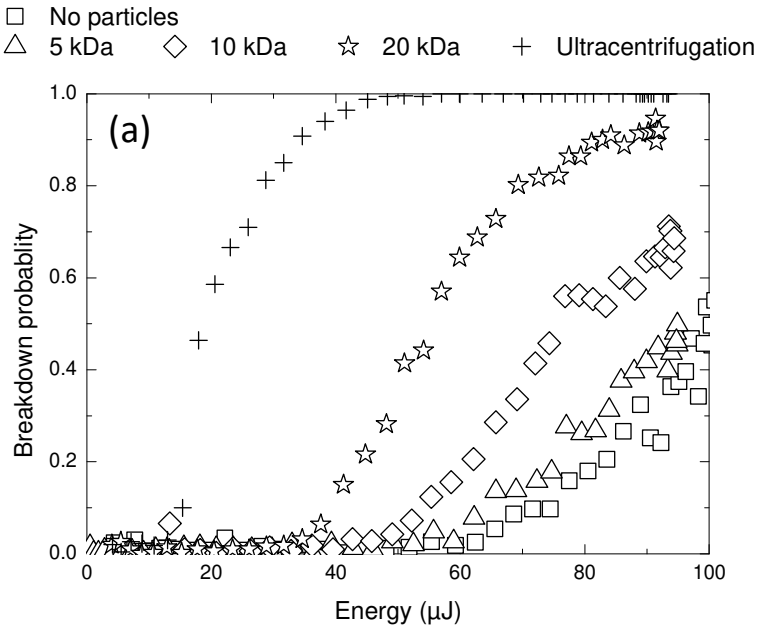

616

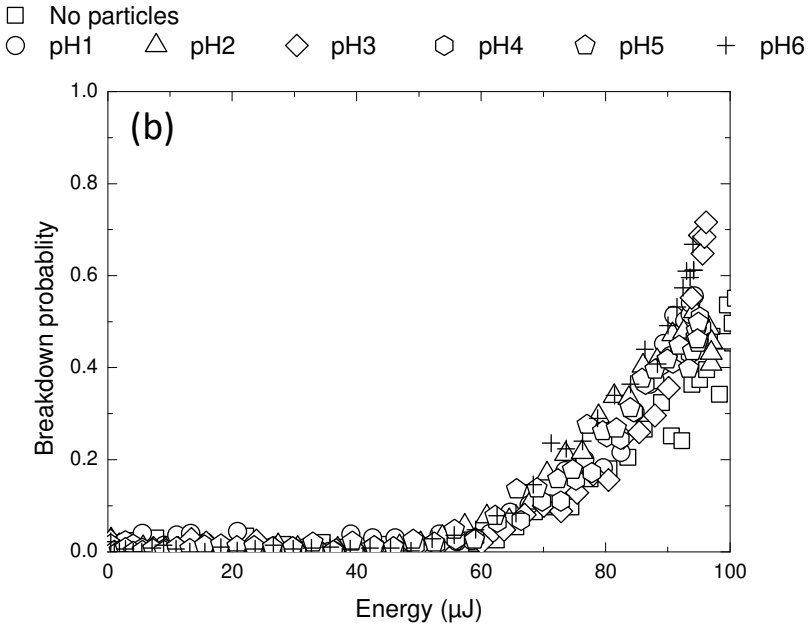

617

618 Figure 6 : Breakdown probability as function of laser energy obtained by LIBD. (a) Comparison
619 between ultrafiltration and ultracentrifugation methods applied on the separation of ZrO_2
620 nanoparticles. (b) Ultrafiltration by 5 kDa at various pH of monoclinic nanoparticles.

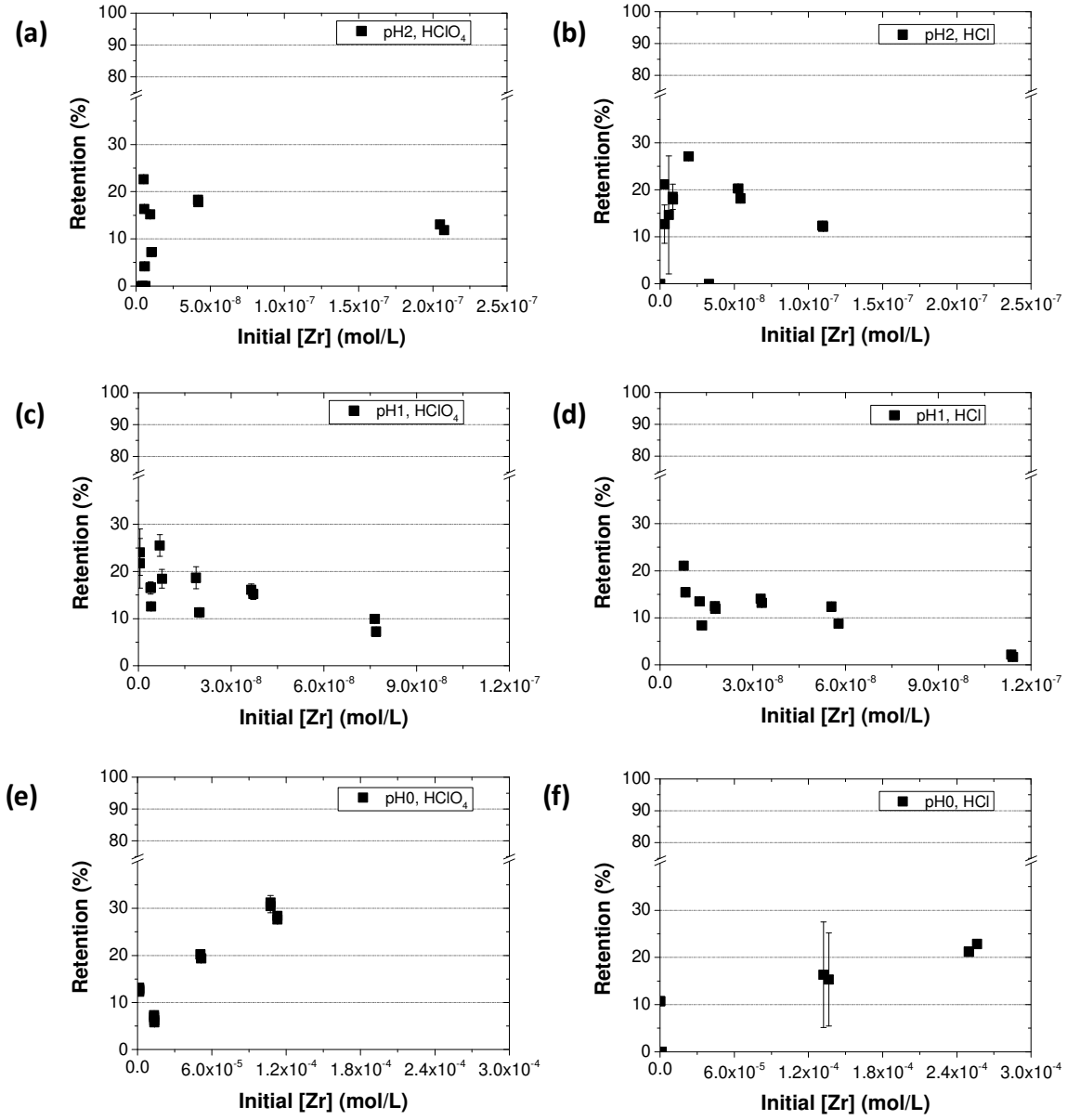

621

622 Figure 7 : The amount of zirconium adsorbed/retained on filter membranes of standard solutions
623 prepared in I=0.01 (a) $HClO_4$ pH 2, (b) HCl pH 2, (c) $HClO_4$ pH 1, (d) HCl pH 1, (e) $HClO_4$ pH 0, (f) HCl pH
624 0 matrices as function of initial standard solution concentrations.

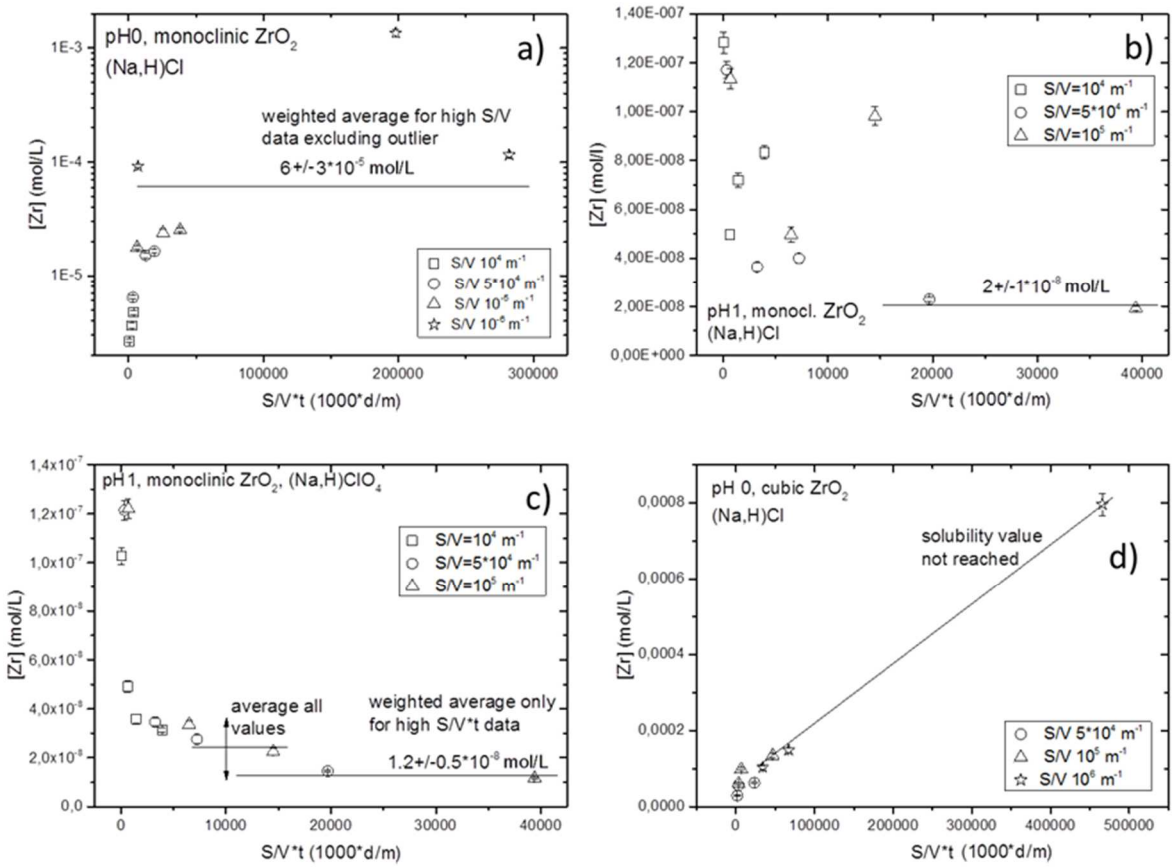

625

626 Figure 8: The total zirconium concentrations plotted against S/V×time and measured in a period of
627 time ranging from 7 days to 400 days of dissolution experiments of monoclinic zirconia in (a) HCl pH
628 0, (b) HCl pH 1 and (c) $HClO_4$ pH 1, and of cubic zirconia in (d) HCl pH 0.

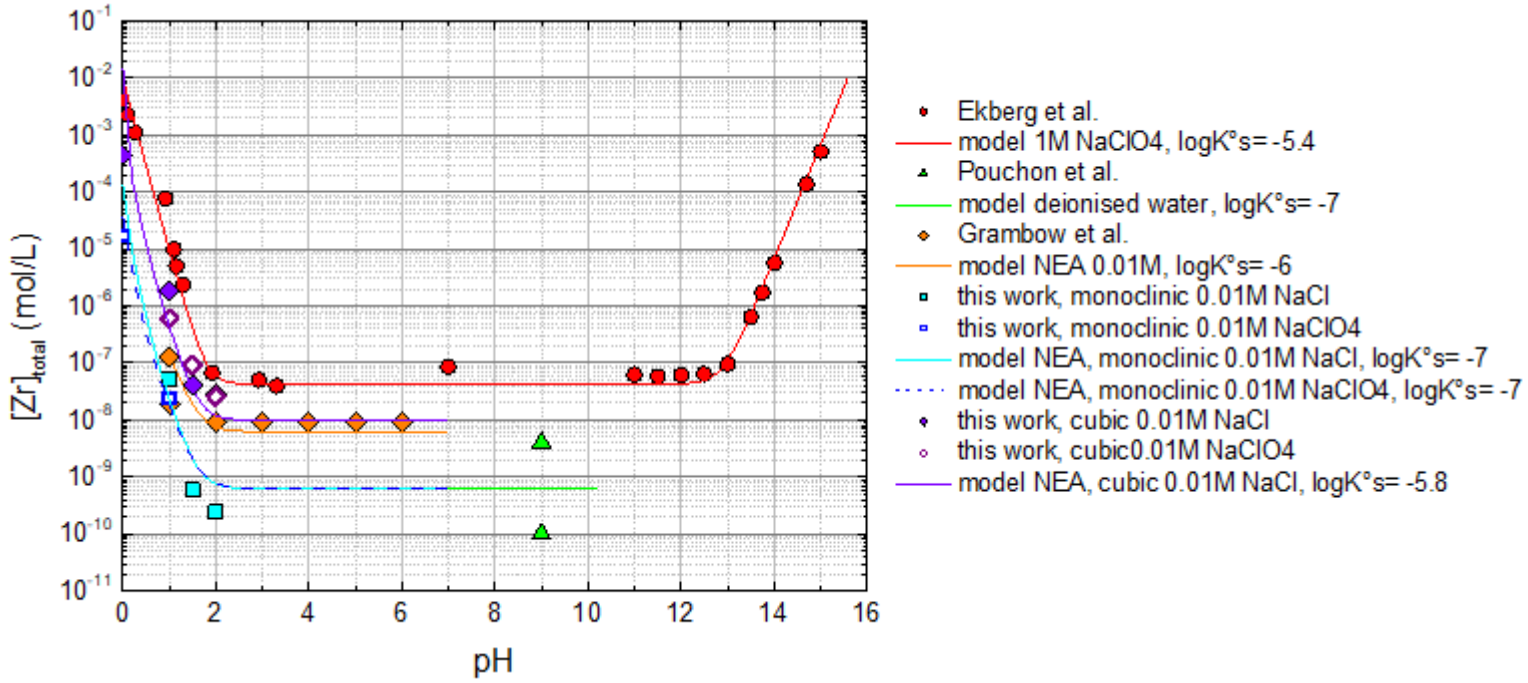

629

630 Figure 9: Comparison of experimental data from this work and in various ionic media from literature with NEA-TDB [20] model, only log K_s^0 values were

631 fitted.

632 **List of Tables**

643

644 Table 1: Experimental conditions : pH-measured values (pH) and converted pH-measured into
645 concentrations of protons (pmH^+) in 10^{-2} mol·L^{-1} NaCl and $NaClO_4$ media, solid phase, ratio of solid
646 surface over volume of solution, and total duration of experiment.

Aqueous medium	**pH**	**pmH^+**	**Solid phase**	**$(S/V)\times10^3$ (m^{-1})**	**Duration (days)**
(Na,H)Cl	2.0	1.96	Monoclinic	10, 1000 2000	396 236
			Cubic	1000, 2000	377
	1.5	1.47	Monoclinic	10, 100	118
			Cubic	10, 100	322
	1.0	0.94	Monoclinic	10, 50, 100	394
			Cubic	10, 50, 100	428
	0	0.15	Monoclinic	10, 50, 100 1000	383 282
			Cubic	50, 100, 1000	466
$(Na,H)ClO_4$	2.0	1.94	Monoclinic	10, 1000 2000	396 236
			Cubic	1000, 2000	377
	1.5	1.46	Monoclinic	10, 100	118
			Cubic	10, 100	322
	1.0	1.03	Monoclinic	10, 50, 100	394
			Cubic	10, 50, 100	428
	0	0.19	Monoclinic	10, 50, 100 1000	383 282
			Cubic	50, 100, 1000	466

647

Table 2: Solubility values of zirconium in presence of monoclinic and cubic zirconia. Solubility constants log K_s^0 of ZrO_2 nanoparticles determination based on Zr-hydrolysis model and ionic strength correction for each solid phase and medium, average values of log K_s^0 for a given medium for each solid phase, and solubility constant for large ZrO_2 phases log $K_s^0(\bar{S}=0)$ calculated from Schindler equation [33]. Quantification limit (QL) ≈10^{-11} mol.L^{-1}. * Solubility constant determined from the maximum zirconium concentration obtained above the quantification limit.

Solid phase	**[Zr] (mol·L^{-1})**	**log K_s^0**	**Average of log K_s^0 for nanoparticles**	**log $K_s^0(\bar{S}=0)$ for large ZrO_2 phases**	**Media**	**pH**
Monoclinic	(1.8±1.2)×10^{-10}	-7.76±0.34	-7.33±0.69	-8.43±0.69	10^{-2} mol·L^{-1} (Na,H)Cl	2±0.1
	(2.3±1.0)×10^{-10}	-8.08±0.20				1.5±0.1
	(2.0±1.0)×10^{-8}	-7.31±0.24				1±0.1
	(6.0±3.0)×10^{-5}	-6.67±0.23				0±0.1
	< QL				10^{-2} mol·L^{-1} (Na,H)ClO_4	2±0.1
	< QL	-8.07*				1.5±0.1
	(1.2±0.5)×10^{-8}	-7.15±0.02				1±0.1
	(3.0±1.0)×10^{-5}	-6.30±0.17				0±0.1
Cubic	(2.4±0.9)×10^{-8}	-5.51±0.14	-5.86±0.36	-7.12±0.35	10^{-2} mol·L^{-1} (Na,H)Cl	2±0.1
	(1.0±3.0)×10^{-8}	-6.32±0.23				1.5±0.1
	(8.0±0.2)×10^{-7}	-5.73±0.17				1±0.1
	(2.7±1.0)×10^{-8}	-5.57±0.16			10^{-2} mol·L^{-1} (Na,H)ClO_4	2±0.1
	(1.4±7.0)×10^{-8}	-6.38±0.12				1.5±0.1
	(4.5±0.5)×10^{-7}	-5.70±0.03				1±0.1
	(1.6±0.5)×10^{-4}	-5.82±0.07				0±0.1

654 Table 3: Number of dissolved monolayers determined from (i) DMSAP and (ii) the crystallographic
655 density, for pH 0 and 2.

656

Solids	pH	Number of dissolved monolayers	
		based on proton exchanged (determined from DMSAP)	determined from the crystallographic site density
Monoclinic ZrO_2	0	0.005	0.001
	2	4×10^{-8}	1.9×10^{-8}
Cubic ZrO_2	0	0.35	0.035
	2	2.3×10^{-5}	2.3×10^{-6}

657